ACS central science

http://pubs.acs.org/journal/acscii

Research Article

A Dual Anchoring Strategy for the Directed Evolution of Improved Artificial Transfer Hydrogenases Based on Carbonic Anhydrase

Alina Stein,[‖] Dongping Chen,[‖] Nico V. Igareta, Yoann Cotelle,* Johannes G. Rebelein,* and Thomas R. Ward*

Cite This: *ACS Cent. Sci.* 2021, 7, 1874−1884

Read Online

ACCESS | Metrics & More | Article Recommendations | Supporting Information

ABSTRACT: Artificial metalloenzymes result from anchoring a metal cofactor within a host protein. Such hybrid catalysts combine the selectivity and specificity of enzymes with the versatility of (abiotic) transition metals to catalyze new-to-nature reactions in an evolvable scaffold. With the aim of improving the localization of an arylsulfonamide-bearing iridium-pianostool catalyst within human carbonic anhydrase II (hCAII) for the enantioselective reduction of prochiral imines, we introduced a covalent linkage between the host and the guest. Herein, we show that a judiciously positioned cysteine residue reacts with a *p*-nitropicolinamide ligand bound to iridium to afford an additional sulfonamide covalent linkage. Three rounds of directed evolution, performed on the dually anchored cofactor, led to improved activity and selectivity for the enantioselective reduction of harmaline (up to 97% *ee* (*R*) and >350 turnovers on a preparative scale). To evaluate the substrate scope, the best hits of each generation were tested with eight substrates. X-ray analysis, carried out at various stages of the evolutionary trajectory, was used to scrutinize (i) the nature of the covalent linkage between the cofactor and the host as well as (ii) the remodeling of the substrate-binding pocket.

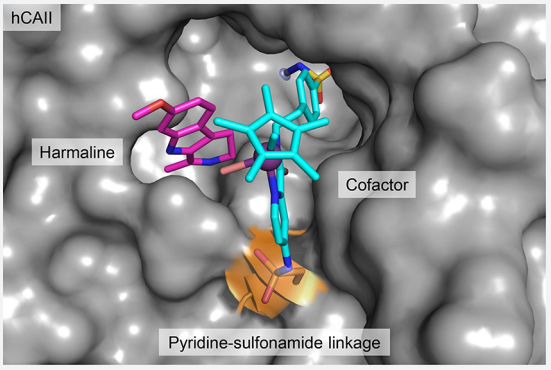

INTRODUCTION

Artificial metalloenzymes (ArMs) expand the repertoire of biocatalyzed reactions.[1−10] ArMs combine attractive features of organometallic catalysts—such as broad substrate scope and large reaction repertoire—with characteristics of enzymes, including high turnover numbers, unrivalled stereoselectivity, and biocompatibility. Such hybrid catalysts result from the incorporation of an abiotic metal cofactor within a protein.[11−16] Four distinct anchoring strategies have been pursued to date: covalent,[17−19] supramolecular,[20−22] dative,[23−25] and metal substitution.[26−28] As the "repurposed active site" seldom snugly matches the structure of the cofactor·substrate complex, the cofactor is poorly localized, potentially limiting the effect of mutations on the catalytic performance of ArMs.[29] With the aim of firmly localizing an abiotic cofactor, several groups have engineered additional interactions between the cofactor and the host protein, ultimately leading to improved activities and selectivities for ArMs based on myoglobin,[30,31] LmrR,[32−35] streptavidin,[36] etc.

To complement our efforts centered around streptavidin-based ArMs, our group has reported the use of human carbonic anhydrase II (hCAII) as a host protein for the assembly and optimization of an artificial transfer hydrogenase[37−39] (ATHase hereafter) and artificial metathase.[40] hCAII provides an attractive scaffold due to its monomeric globular structure (30 kDa), high affinity for aromatic sulfonamides, and large funnel-shaped hydrophobic access to the active site.[41,42] Thanks to its monomeric nature, hCAII can readily be displayed on *Escherichia coli*'s outer membrane, significantly simplifying the ArM's assembly and the whole-cell screening procedure. In a previous study, we identified cofactor **1** (Figure 1a) as a promising cofactor for the transfer hydrogenation using wild-type hCAII (hCAII^{WT}) as a protein scaffold.[39] Enantiopure amines represent attractive targets both as pharmaceutical ingredients and agrochemicals.[43−46] Following a seminal report in 2011,[47] imine reductases have firmly highlighted their versatility for the production of enantiopure amines.[48−51] These complement homogeneous catalysts for the reduction of prochiral enamines and imines.[52−54] Capitalizing on our previous efforts in ATHases, we set out to introduce a covalent anchor between the IrCp* cofactor and hCAII. We hypothesized that the resulting firm localization of the cofactor may positively affect both the turnover numbers (TONs) and the stereoselectivity of the resulting ATHase.

Received: July 8, 2021
Published: November 11, 2021

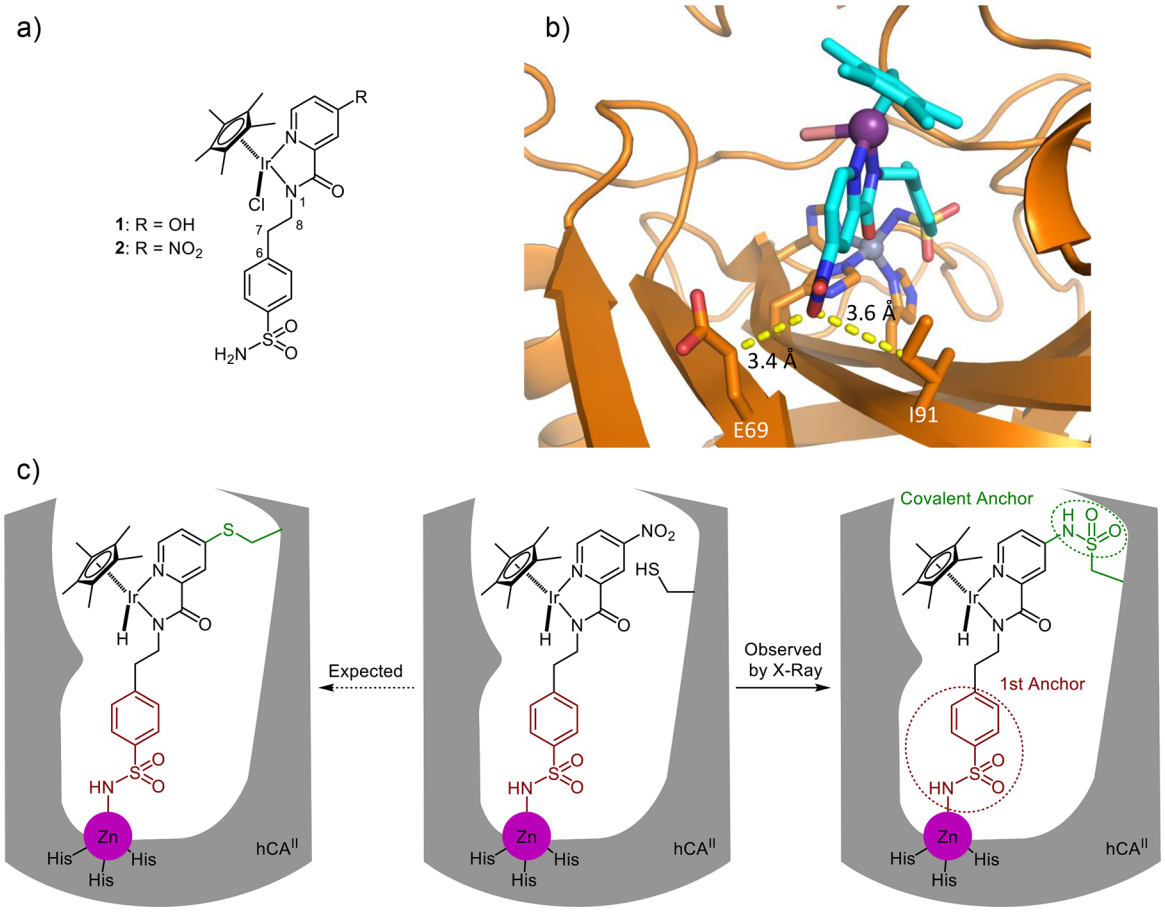

Figure 1. Strategy to assemble dually anchored ArMs. (a) Structure of the cofactors **1**−**2**, (b) X-ray structure of cofactor **2** (depicted as sticks, Ir and Zn as color-coded spheres) bound to hCA^{WT} (depicted as cartoon representation). Distances between the O_{nitro} and the residue glutamate E69 and isoleucine I91 (depicted as sticks) are highlighted, (c) Schematic representation of the expected and observed dual anchoring within engineered hCAII^{E69C} and hCAII^{I91C}.

Building on the abundant literature covering ligation of cysteines with electrophiles[55] including maleimides,[56] nitro pyridines,[57] halogenoalkanes,[58] alpha-halocarbonyls,[59] Mukaiyama reagents,[60] and sulfones,[61] we envisioned engineering a suitably positioned cysteine residue that would undergo a nucleophilic addition on the cofactor bearing an electrophilic moiety. Herein, we report on our efforts to design and evolve an ATHase equipped with a dual-anchoring system.

DESIGN OF A DUAL-ANCHORING STRATEGY FOR CARBONIC ANHYDRASE

Building on our previous hCAII-based ATHase,[39] the requirements for the cofactor design were set as follows: (i) an arylsulfonamide moiety for anchoring to hCAII, (ii) an ethyl spacer between the anchor and the IrCp* moiety, (iii) a picolinamide chelate for increased transfer hydrogenation activity,[62] and (iv) an electrophilic substituent on the pyridine, susceptible to nucleophilic attack by a suitably positioned cysteine (Figure 1). We envisioned that cofactor **2** would efficiently bind to hCAII thanks to the arylsulfonamide linker and would be further anchored via a nucleophilic aromatic substitution (S_NAr) with a suitably positioned cysteine residue present in the protein vestibule (Figure 1c). Moreover, we hypothesized that the S_NAr may further increase the activity of the IrCp* picolinamide complex by increasing the electron-donating ability of the ligand.[63] Cofactor **2** was synthesized in two steps from commercially available starting materials (Scheme S1). Next, hCAII^{WT} was crystallized by sitting drop vapor diffusion, and the crystals were cross-linked with glutaraldehyde prior to soaking with cofactor **2** (see Supporting Information). The resulting X-ray diffraction data were solved at 1.41 Å resolution. Inspection of the X-ray structure of **2**·hCAII^{WT} reveals that both glutamate 69 (E69) and isoleucine 91 (I91) residues lie closest to the electrophilic nitro group of the picolinamide. The shortest contacts to one oxygen of the nitro group to cofactor **2** for these two residues are C_γ of E69 and $C_{\gamma1}$ of I91 (3.4 and 3.6 Å, respectively, Figure 1b). Accordingly, we expressed and purified the single mutants hCAII^{E69C} and hCAII^{I91C} and evaluated their catalytic performance toward the transfer hydrogenation of harmaline **3** and dihydroisoquinolinium **4** precursor to crispine A **4**-H_2. ATHases **1**·hCAII^{WT}, **1**·hCAII^{E69C}, and **1**·hCAII^{I91C} perform poorly for the reduction of substrate **3** (Table S18). In contrast, ATHases **2**·hCAII^{WT}, **2**·hCAII^{E69C}, and **2**·hCAII^{I91C} catalyze the enantioselective reduction of both substrates. Strikingly, the position of the cysteine residue affects the resulting enantioselectivity: for both substrates, opposite enantiomers are preferentially produced in the presence of **2**·hCAII^{E69C} and **2**·hCAII^{I91C}, respectively (Table 1). To assemble the ArMs, cofactor **2** (0.1 mM) and hCAII$^{WT,\ E69C\ or\ I91C}$ (0.1 mM) were incubated (6 h) at room temperature using carbonate buffer (50 mM, pH 9.4). Transfer hydrogenation was performed using substrate (2 mM) and

https://doi.org/10.1021/acscentsci.1c00825
ACS Cent. Sci. 2021, 7, 1874−1884

Table 1. Catalytic Performance of ATHases Constructed by Anchoring Cofactor 2 to hCAII^{WT}, hCAII^{E69C}, and hCAII^{I91C}[a]

	Protein	Substrate	Yield (%)	TON	*ee* (%)
1	WT	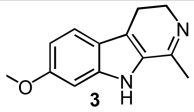	68	136	26 (*R*)
2	E69C		66	132	50 (*R*)
3	I91C	**3**	66	132	38 (*S*)
4	WT	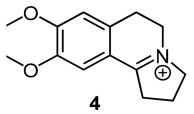	6	12	7
5	E69C		13	26	-50
6	I91C	**4**	30	60	15

[a]Reactions were performed for 16 h using hCAII (10 μM), cofactor **2** (10 μM), and substrate (2 mM) in MOPS/$NaHCO_2$ buffer (pH 7.4, 0.34 M, 0.85 M).

ArMs (10 μM) in MOPS buffer containing $NaHCO_2$ (1 M) as the hydride source. Reduction of harmaline **3** using **2**·hCAII^{WT} gave (*R*)-**3**-H_2 with a good yield (68%, after 16 h) and a moderate enantioselectivity (26% *ee*). In contrast, **2**·hCAII^{E69C} gave (*R*)-**3**-H_2 with a comparable yield (66%) but with an increased *ee* = 50%. Interestingly, **2**·hCAII^{I91C} also gave a good yield (66%) and a reverse *ee* = −38% for (*S*)-**3**-H_2 (Table 1, Entry 1−3). The difference in enantioselectivity suggests different binding poses for harmaline in the larger binding pocket of **2**·hCAII^{I91C} compared to **2**·hCAII^{E69C} (Figures S3 and S5). More strikingly, the reduction of iminium **4** by **2**·hCAII^{WT} gave a low conversion (6%) and hardly any enantioselectivity (Table 1, Entry 4). In contrast, **2**·hCAII^{E69C} led to a slightly higher yield (13%) and *ee* (−50%) (Table 1, Entry 5). Mutant **2**·hCAII^{I91C} gave a higher yield (30%) but low enantioselectivity (15%, Table 1, Entry 6). Taken together, these results highlight the power of the dual-anchoring strategy, giving rise to an increased enantioselectivity for substrates **3** and **4** compared to the parent hCAII^{WT}. To further improve the catalytic performance of the dually anchored ATHases, we relied on directed evolution.[64−66]

To confirm the dual anchoring of the cofactor **2** within hCAII^{E69C} and hCAII^{I91C}, the two variants were incubated with cofactor **2** (16 h, pH 9.4, 50 mM $(NH_4)_2CO_3$). The unbound cofactor **2** was removed, and the buffer was exchanged (25 mM Tris-HCl, pH 7.4) by ultrafiltration. The resulting ArMs were crystallized by sitting drop vapor diffusion (see Supporting Information). To our delight, the crystals diffracted to a good resolution for **2**·hCAII^{E69C} (1.51 Å) and for **2**·hCAII^{I91C} (1.04 Å). The electron density highlights the cofactor's localization within hCAII^{E69C} (Figure S1) and hCAII^{I91C} (Figure 3b,c). As observed for **2**·hCAII^{WT}, the arylsulfonamide anchor of cofactor **2** is bound to the zinc ion of hCAII. An additional bond was identified between the picolinamide moiety and the engineered cysteine residues. Unexpectedly, the well-resolved electron density revealed the presence of a pyridine−sulfonamide linkage (Figures 3b,c and S1b and S2b), rather than the anticipated thioether moiety (Figure 1c). For **2**·hCAII^{I91C}, the pyridine−sulfonamide bond

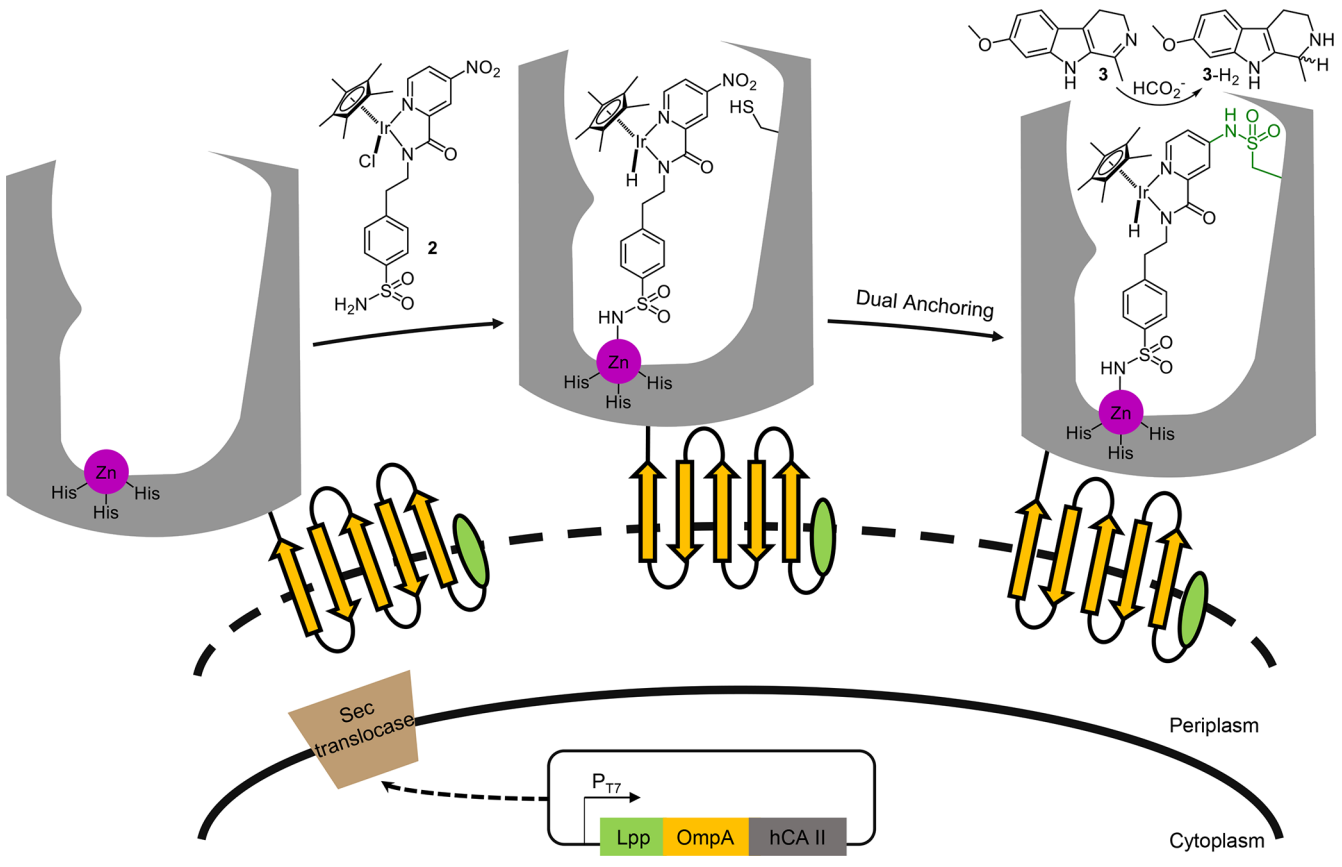

Figure 2. *In cellulo* assembly of artificial transfer hydrogenases (ATHases). hCAII is displayed on the cell surface of *E. coli* by fusion to a truncated lipoprotein and the outer membrane protein A (Lpp-OmpA). Following incubation with the sulfonamide-bearing IrCp* pianostool complex **2**, the resulting ArM catalyzes the enantioselective reduction of harmaline **3** in the presence of $NaHCO_2$ as the hydride source.

https://doi.org/10.1021/acscentsci.1c00825
ACS Cent. Sci. 2021, 7, 1874−1884

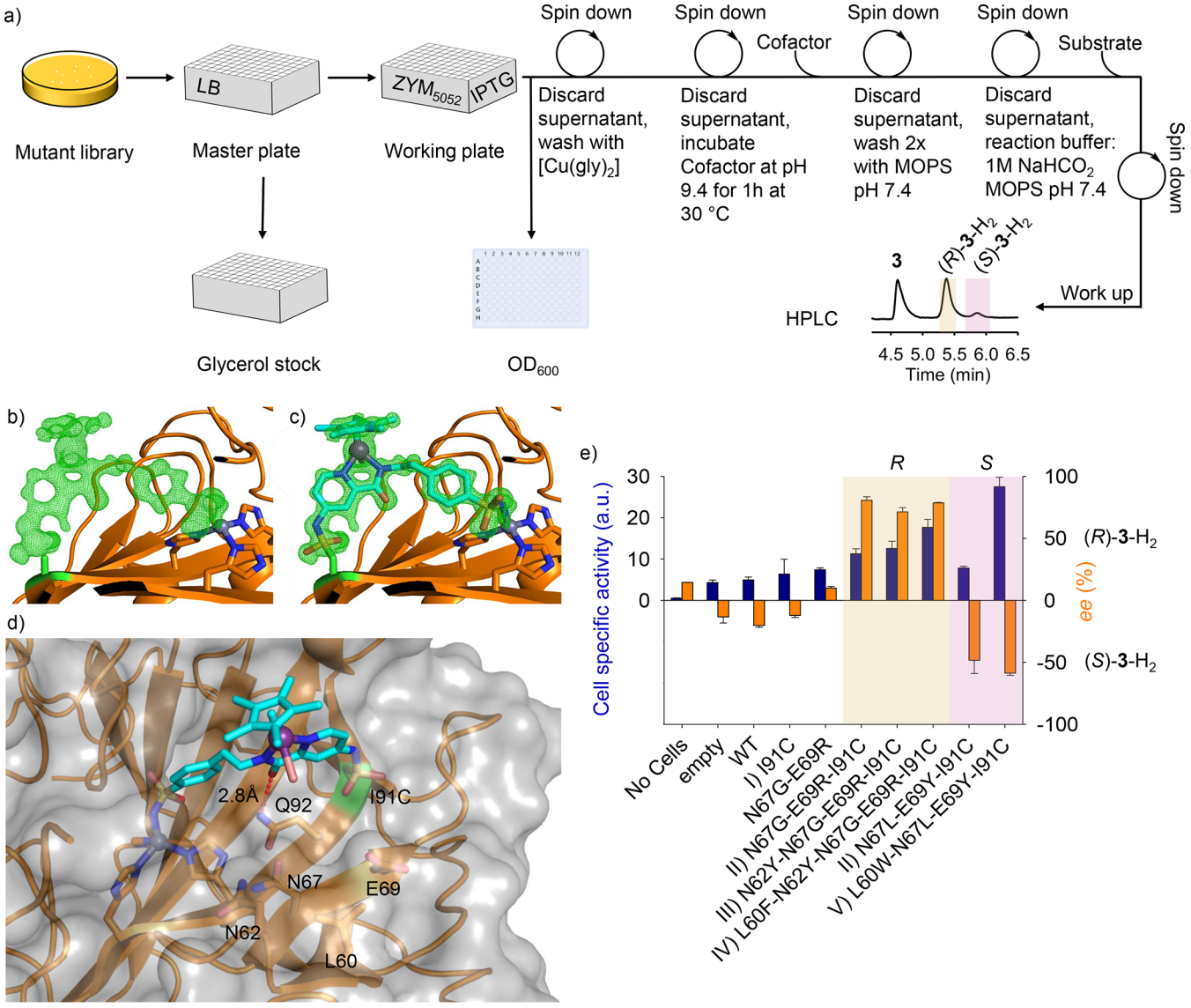

Figure 3. Directed evolution of ArMs resulting from the dual anchoring of cofactor **2**. (a) A streamlined screening workflow was developed that enables expression of hCAII mutants and subsequent evaluation of their activity and selectivity in a 96-well plate format. See Supporting Information for a detailed description of the workflow. (b–d) X-ray characterization of the ATHase **2**·hCAII^{I91C}. (b) Fo-Fc difference map displayed as green mesh at 3σ without and (c) with cofactor **2**. (d) hCAII^{I91C} is depicted as a transparent gray surface and orange cartoon. Amino acids in the proximity of the cofactor are highlighted as sticks and labeled; the H-bond between Q92 and cofactor **2** is depicted as red dashes. The five residues (L60, N62, N67, E69, and Q92) closest to the catalytic iridium in hCAII^{I91C} were randomized by site-saturation mutagenesis. (e) Summary of the results of the directed evolution for the production of tetrahydroharmine **3**-H$_2$. For each round of site-saturation mutagenesis, the cell-specific activity (product concentration/O.D.) and the enantiomeric excess (*ee*) of selected mutants are displayed as bar chart (TON, dark blue; *ee*, orange; enantiomer: *R*, positive, highlighted in gold; *S*, negative, highlighted in pink). Data are presented as the average of three independent replicate cultures and include the standard deviation. For the site-saturation library of Q92, no further improved mutant was identified.

is fully formed, resulting in a complete occupancy (100%) for the IrCp*(picolinamide) moiety (Figures 3c and S2b and S2e). For **2**·hCAII^{E69C}, the IrCp*(picolinamide) moiety with the pyridine–sulfonamide linkage has a lower occupancy (~70%) (Figure S1). Two additional cofactor positions with a free cysteine E69C were refined (Figure S1c). The incomplete formation of the pyridine–sulfonamide bond for hCAII^{E69C} may be caused by the somewhat unfavorable geometry that cofactor **2** has to adopt to form the pyridine–sulfonamide linkage (Figure S3). The dihedral angle between C6–C7–C8–N1 serves as an indicator for the strain on cofactor **2**. Within hCAII^{E69C}, the dually anchored cofactor **2** has an acute dihedral angle (102.2°), which is significantly smaller than the dihedral angle observed for the noncovalently bound cofactor **2** in hCAII^{WT} (158.6°). The dihedral angle for **2** in hCAII^{I91C} (134.0°) is closer to the angle of **2** in hCAII^{WT} (158.6°) suggesting a more relaxed geometry of **2** in hCAII^{I91C}. The observed difference of the dihedral angles of **2** in hCAII^{E69C} and hCAII^{I91C} might explain the difference between the incomplete and quantitative formation of the pyridine–sulfonamide bond for these two hCAII mutants, respectively.

Compared to **2**·hCAII^{WT}, the presence of the pyridine–sulfonamide linkage leads to the relocation of the Ir-picolinamide complex in hCAII^{I91C}, providing slightly more space for substrate binding (Figures S3 and S5). The Ir-ion of ATHase **2**·hCAII^{I91C} is displaced (1.0 Å), and the N2 of the

https://doi.org/10.1021/acscentsci.1c00825
ACS Cent. Sci. 2021, 7, 1874–1884

nitro precursor is shifted (3.4 Å) in **2**·hCAII^{I91C} compared to **2**·hCAII^{WT} (Figure S4). Cofactor **2** is stabilized via H-bonds with glutamine 92 (Q92) and threonine 198 (T198) and by π-stacking with phenylalanine (F130) in hCAII^{I91C} (Figure S6). In all three X-ray structures of **2**·hCAII$^{WT,\ E69C\ and\ I91C}$, the Ir in **2** has an (*S*)-configuration. In contrast to previous reports on ATHases, the absolute configuration of the metal does not correlate with the configuration of the products.[67] Indeed, both **2**·hCAII^{E69C} and **2**·hCAII^{I91C} contain cofactor **2** with an (*S*)-configuration at the Ir−Cl, but convert substrate **3** and **4** preferentially to opposite enantiomers.

Having established a powerful method to dually anchor the cofactor **2** to hCAII scaffolds bearing a judiciously positioned cysteine residue, we set out to optimize the ATHase activity by directed evolution.[64−66]

DIRECTED EVOLUTION

To improve the activity of ATHases based on the dual-anchoring strategy, we selected hCAII^{I91C} as a scaffold for directed evolution. The selection of hCAII^{I91C} over hCAII^{E69C} is based on the following considerations: (i) the bioconjugation is quantitative, thus affording single and well-defined localization of the cofactor **2** within the "active site", and (ii) more space is available for the prochiral substrate to approach the Ir−H moiety. To streamline the directed evolution, we selected an *E. coli* surface display for hCAII.[39] This strategy was favored over the periplasmic compartmentalization in light of the following factors: (i) the cofactor concentrations are roughly similar—as determined by ICP-MS—and (ii) the accessibility for the substrate is coupled with a defined reaction environment (i.e., extracellular versus peptidoglycan environment).[39] For *E. coli* surface display, hCAII was fused at its *N*-terminus with a truncated *E. coli* lipoprotein Lpp (residues 1−9), followed by the first five β-sheets of OmpA (residues 46−159, Figure 2). Initial experiments were performed with hCAII^{WT} and hCAII^{I91C} evaluating the effect of varying concentrations of cofactor **2** in the presence of either substrate **3** or **4**. In line with the reactions performed with purified hCAII samples (Table 1), the conversion of substrate **3** was higher than that of substrate **4**. Accordingly, harmaline **3** was selected as the substrate for the directed evolution campaign. To minimize the background reaction resulting from unspecifically bound cofactor **2** (e.g., in the presence of *E. coli* bearing an empty plasmid), its concentration was set to 5 μM (Figure S7).

Next, we designed site-saturation mutagenesis libraries for hCAII^{I91C}, focusing on the five closest residues to the chloride ligand of **2** as determined in the X-ray structure of **2**·hCAII^{I91C} (Figure 3b). The closest lying positions are L60, N62, N67, E69, and Q92. To minimize the screening effort, we relied on a "small-intelligent" focused library approach by combining NDT, VMA, and TGG codons.[68] We omitted the ATG codon to exclude methionine, thus affording a nonredundant library encoding 19 amino acids. We developed a workflow for the growth, expression, and catalysis by *E. coli* displaying hCAII mutants in a 96-well format (Figure 3a). After induction of hCAII, followed by overnight expression (30 °C), the cells were harvested by centrifugation and washed with a [Cu(gly)$_2$] buffer to oxidize traces of thiols.[69,70] Next, the cells were resuspended in a buffer (pH 9.4, 50 mM $(NH_4)_2CO_3$) containing the cofactor **2** and incubated (1 h at 30 °C) to afford the dually anchored ArMs on the cell surface. The supernatant was removed by centrifugation, and the cells were resuspended in the reaction buffer (pH 7.4, 0.4 M MOPS) containing substrate **3** (50 μM) and $NaHCO_2$ (1 M). The 96-well plate was then shaken (16 h at 30 °C, 300 rpm). Cells were sedimented by centrifugation, and the supernatant was transferred to a reaction tube (1.5 mL) for workup. Finally, each sample was analyzed by supercritical fluid chromatography (SFC, using 2-methyl indoline as an internal standard) to determine the product concentration and enantioselectivity. This procedure enables the screening of hundreds of mutants per week, substantially increasing the throughput compared to the conventional workflow that relies on purified mutants. The first round of directed evolution was performed by constructing a combinatorial library, mutating simultaneously asparagine 67 (N67) and glutamate 69 (E69), which are located 5.6 and 6.5 Å from the chloride ligand of cofactor **2**, respectively. Upon screening (>650 colonies), we identified two mutants displaying an increased cell-specific activity compared to **2**·hCAII^{WT} and **2**·hCAII^{I91C}. The ATHase **2**·hCAII$^{N67G\text{-}E69R\text{-}I91C}$ had a higher cell-specific activity (1.8 ± 0.2 (average ± s.d.) fold) compared to **2**·hCAII^{I91C} and an enhanced enantioselectivity for (*R*)-**3**-H_2 (80.0 ± 2.9% *ee*). To explore the influence of the pyridine−sulfonamide anchor, we expressed hCAII$^{N67G\text{-}E69R}$ lacking the I91C mutation. The corresponding **2**·hCAII$^{N67G\text{-}E69R}$, afforded a markedly reduced *ee* (10.0 ± 1.2%) and a reduced activity compared to **2**·hCAII$^{N67G\text{-}E69R\text{-}I91C}$ for the reduction of harmaline **3**. Interestingly, the second identified mutant **2**·hCAII$^{N67L\text{-}E69Y\text{-}I91C}$ afforded (*S*)-**3**-H_2 with a slightly higher cell-specific activity compared to **2**·hCAII^{I91C} (1.2 ± 0.1-fold) and a moderate *ee* (−48.0 ± 10.7%). Two additional rounds of directed evolution at positions L60 and N62 afforded a quintuple mutant hCAII$^{L60F\text{-}N62Y\text{-}N67G\text{-}E69R\text{-}I91C}$, which displayed a higher cell-specific activity (2.8 ± 0.3-fold) and a similar *ee* (79.0 ± 0.4%) for enantiomer (*R*)-**3**-H_2 compared to **2**·hCAII^{I91C}. Starting from the (*S*)-selective ATHase **2**·hCAII$^{N67L\text{-}E69Y\text{-}I91C}$, the directed evolution campaign afforded the quadruple mutant hCAII$^{L60W\text{-}N67L\text{-}E69Y\text{-}I91C}$ which displayed the highest cell-specific activity (4.3 ± 0.4 fold) compared to hCAII^{I91C} and an improved *ee* (−59 ± 1.8%) for (*S*)-**3**-H_2 (Figure 3e). The purified mutants hCAII$^{N62D\text{-}N67L\text{-}E69Y\text{-}I91C}$ and hCAII$^{L60W\text{-}N62D\text{-}N67L\text{-}E69Y\text{-}I91C}$ displayed higher activities than the parent hCAII$^{N67L\text{-}E69Y\text{-}I91C}$ for several substrates as summarized below (Table 2). All mutants resulting from the site-saturation mutagenesis library at position Q92 displayed a decreased activity. We hypothesize that the H-bond interaction between Q92 and the cofactor **2** plays an important role in maintaining the cofactor's position within the active site of the ATHase to favor the pyridine−sulfonamide linkage (Figures 3b and 4).

The hCAII mutant proteins were expressed in 2 L cultures and purified (up to 100 mg of lyophilized protein). Transfer hydrogenation was then performed on harmaline **3** with purified proteins and cofactor **2** to validate the results obtained from the whole-cell experiments. From the *in vitro* validation, we can draw the following conclusions: (i) TON and stereoselectivity of the evolved ATHases are higher than the parent cofactor **2** and **2**·hCAII^{WT} (Table 2, Entry 2−3), confirming the efficiency of our strategy, (ii) concerning (*R*)-selectivity, **2**·hCAII$^{N67G\text{-}E69R\text{-}I91C}$ is the best mutant, affording enantiomer (*R*)-**3**-H_2 (96% *ee*, 451 TON; Table 2, Entry 5), (iii) for the best ATHase for (*S*)-**3**-H_2, only moderate *ee* are observed, with **2**·hCAII$^{N67L\text{-}E69Y\text{-}I91C}$ (−62% *ee*) and **2**·hCAII$^{L60W\text{-}N67L\text{-}E69Y\text{-}I91C}$ (−49% *ee*; Table 2, Entry 8−9), (iv)

https://doi.org/10.1021/acscentsci.1c00825
ACS Cent. Sci. 2021, 7, 1874−1884

Table 2. Selected Catalytic Results Obtained with Purified 2·hCAII^{mutants} for the Transfer Hydrogenation of Harmaline 3[a]

	mutants	TON	*ee* (%)
1	none	311	0
2	hCAII	149	31 (*R*)
3	hCAII^{E69C}	278	48 (*R*)
4	hCAII^{I91C}	265	39 (*S*)
5	hCAII$^{N67G\text{-}E69R\text{-}I91C}$	451	96 (*R*)
6	hCAII$^{N62Y\text{-}N67G\text{-}E69R\text{-}I91C}$	460	73 (*R*)
7	hCAII$^{L60F\text{-}N62Y\text{-}N67G\text{-}E69R\text{-}I91C}$	415	74 (*R*)
8	hCAII$^{N67L\text{-}E69Y\text{-}I91C}$	458	62 (*S*)
9	hCAII$^{L60W\text{-}N67L\text{-}E69Y\text{-}I91C}$	221	9 (*S*)
10	hCAII$^{N67G\text{-}E69R\text{-}I91C}$[b]	375	97 (*R*)
11	hCAII$^{L60W\text{-}N67L\text{-}E69Y\text{-}I91C}$[b]	430	43 (*S*)

[a]Reactions were performed over 16 h using hCAII (10 μM), cofactor **2** (10 μM), and substrate (5 mM) in MOPS/$NaHCO_2$ buffer (pH 7.4, 0.34 M, 0.85 M). Values are the mean values of duplicate experiments. [b]Experiments were performed on a preparative scale with 0.5 mmol of harmaline **3**.

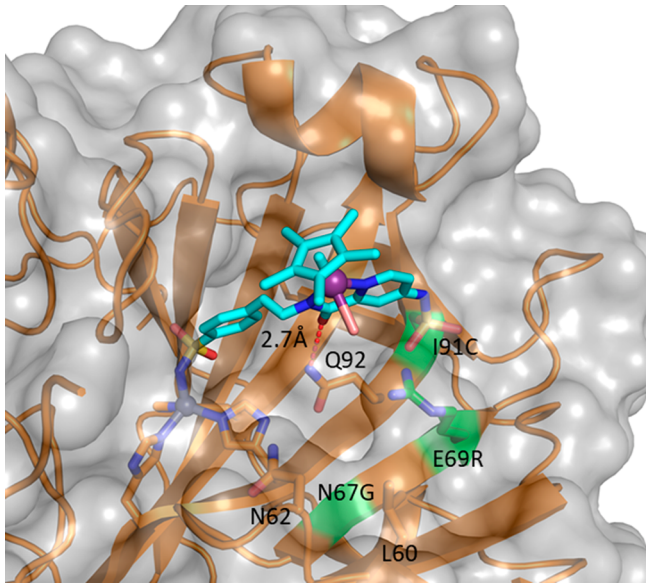

Figure 4. Crystal structure of the evolved **2**·hCAII$^{N67G\text{-}E69R\text{-}I91C}$. The protein is depicted as an orange cartoon and as a transparent gray surface. The cofactor **2** is displayed in color-coded sticks, and Ir-atoms and Zn-atoms are depicted as purple and gray spheres, respectively. Amino acids in the proximity of the cofactor are highlighted as green sticks, labeled, mutated amino acids are highlighted in green, and the H-bond between Q92 and cofactor **2** is depicted as red dashes.

compared to **2**·hCAII$^{N67G\text{-}E69R\text{-}I91C}$, a reduced enantioselectivity was observed for the third- and fourth-generation ArMs. For the (*S*)- but also for the (*R*)-selective ArMs, the *in vitro* activity deviates from the observed whole cell transfer hydrogenation. *In vitro*, we observed that **2**·hCAII$^{N67L\text{-}E69Y\text{-}I91C}$ (458 TON) is more active than **2**·hCAII$^{L60W\text{-}N67L\text{-}E69Y\text{-}I91C}$ (221 TON) this activity profile contrasts with the whole cell assays. These observations suggest that the expression levels of hCAII$^{N67L\text{-}E69Y\text{-}I91C}$ and hCAII$^{L60W\text{-}N67L\text{-}E69Y\text{-}I91C}$ may differ from each other on the surface of *E. coli*.

Next, we performed the transfer hydrogenation on a preparative scale in the presence of harmaline **3** (0.5 mmol) with **2**·hCAII$^{N67G\text{-}E69R\text{-}I91C}$ and **2**·hCAII$^{L60W\text{-}N67L\text{-}E69Y\text{-}I91C}$ (0.2 mol %). The ATHase **2**·hCAII$^{N67G\text{-}E69R\text{-}I91C}$ performs very well (97% *ee*, 75% isolated yield, 84 h) for (*R*)-**3**-H_2, and ArM **2**·hCAII$^{L60W\text{-}N67L\text{-}E69Y\text{-}I91C}$ afforded (*S*)-**3**-H_2 with good yield and moderate *ee* (86% yield, −43% *ee*, 84 h). Relying on hCAII^{I91C} as a starting point, the directed evolution of a dually anchored ATHase led to the identification of significantly improved artificial metalloenzymes, both in terms of activity (up to 451 TONs) and selectivity (up to 97% ee for (*R*)-**3**-H_2 and −62% ee for (*S*)- **3**-H_2).

We attempted to crystallize the complexes of cofactor **2** bound to the best mutant of each directed evolution round. The most (*R*)-selective ATHase **2**·hCAII$^{N67G\text{-}E69R\text{-}I91C}$ afforded crystals suitable for X-ray analysis. The overall structures of **2**·hCAII^{I91C} and **2**·hCAII$^{N67G\text{-}E69R\text{-}I91C}$ are virtually identical, reflected by a C_α RMSD (0.340 Å). Moreover, the position of cofactor **2**, including the pyridine−sulfonamide linkage resulting from the dual anchoring, the interactions between hCAII$^{N67G\text{-}E69R\text{-}I91C}$, and the protein as well as the (*S*)-configuration of the Ir−Cl, is the same in these two mutants (Figures S4c and S6d). These observations confirm that the dual anchoring locks the cofactor **2** in a defined configuration and position. On the one hand, the mutation of asparagine N67 to glycine generates more space (63.7 Å^3)[71] for the substrate to approach the Ir−H moiety. On the other hand, the exchange of glutamate E69 by a cationic arginine might lead to cation-π interactions with the electron-rich substrate **3**. We thus hypothesize that mutations N67G and E69R may improve the binding of the substrate, thereby giving rise to increased TONs and enantioselectivity (Table 2 and 3). Because of the dual anchoring of cofactor **2**, N67 and E69 are not needed for

Table 3. Mass Spectrometry Analysis of Selected ATHases[e]

Native MS

Protein	M_{obs} main peak (Da)	M_{calc} apoprotein[a] (Da)	M_{calc} ATHase[b] (Da)
2 · hCAII^{WT}	29836.9	29181.2	29838.3
2 · hCAII^{E69C}	29812.1	29155.3	29812.4
2 · hCAII^{I91C}	29827.0	29171.2	29828.3
2 · hCAII$^{N67G\text{-}E69R\text{-}I91C}$	29797.7	29141.3	29798.4

Denaturing MS

Protein	M_{obs} (Da)	M_{calc} apoprotein[c] (Da)	M_{calc} ATHase[d] (Da)
2 · hCAII^{WT}	29098.2	29097.8	29772.9
2 · hCAII^{E69C}	29749.0	29071.9	29747.0
2 · hCAII^{I91C}	29763.9	29087.8	29762.9
2 · hCAII$^{N67G\text{-}E69R\text{-}I91C}$	29733.5	29057.9	29733.0

[a]Protein mass plus Zn (65.4 Da) and one H_2O (18.0 Da). [b]Protein mass plus Zn (65.4 Da) and cofactor **2** without Cl (675.1 Da). [c]Protein mass without Zn. [d]Protein mass plus cofactor **2** without Cl (675.1 Da). [e]Similar masses are highlighted in light red.

https://doi.org/10.1021/acscentsci.1c00825
ACS Cent. Sci. 2021, 7, 1874−1884

cofactor binding, as previously described for the computational improvement of the hCAII binding pocket.[37]

COVALENT ANCHORING

As pointed out by an insightful referee, Flemming and co-workers reported that a sulfonamide linkage was formed as a product resulting from the photoreduction of an aromatic nitro group which was trapped by a thiol, followed by redox chemistry at both the nitrogen and sulfur atoms.[72]

In order to confirm that the bioconjugation step is not the result of photoreduction caused by the X-ray beam, the ATHases **2**·hCAII^{E69C}, **2**·hCAII^{I91C}, and **2**·hCAII$^{N67G\text{-}E69R\text{-}I91C}$ as well as the control ATHase **2**·hCAII^{WT} were subjected to MS analysis.

(i) Under native MS conditions, **2**·hCAII^{WT}, **2**·hCAII^{E69C}, **2**·hCAII^{I91C}, and **2**·hCAII$^{N67G\text{-}E69R\text{-}I91C}$ afford, after deconvolution, a main mass signal at 29836.9 Da, 29812.1 Da, 29827.0 Da, and 29797.7 Da, respectively (Table 3 and Figures S22−S25). These masses correspond to the ATHases (hCAII plus cofactor **2**). To further investigate the formation of the sulfonamide linkage, cofactor **2** and hCAII$^{N67G\text{-}E69R\text{-}I91C}$ were incubated in the dark and under ambient light. Native MS revealed almost identical masses, either with or without light: 29797.7 and 29797.8 Da, respectively (Figures S25 and S26). We thus conclude that the formation of the covalent sulfonamide linkage does not require light and is not the result of X-ray photodamage.

(ii) Under denaturing MS conditions, **2**·hCAII^{E69C}, **2**·hCAII^{I91C}, **2**·hCAII$^{N67G\text{-}E69R\text{-}I91C}$ afford signals at 29749.0, 29763.9, and 29733.5 Da, respectively (Table 3 and Figures S27−S30). These correspond to the mass of the bioconjugates, minus the Zn ion. For the above ArMs, a mass of ∼675 Da was observed for cofactor **2** under native and denaturing conditions. This corresponds to the cofactor **2** without the Cl ion. This confirms that cofactor **2** remains tightly bound to hCAII^{E69C}, hCAII^{I91C}, and hCAII$^{N67G\text{-}E69R\text{-}I91C}$, despite the loss of the Zn-sulfonamide dative bond under denaturing conditions. For the ArM lacking the covalent sulfonamide linkage (i.e., **2**·hCAII^{WT}), only the mass of apo hCAII^{WT} (29098.2 Da, minus the Zn ion and no cofactor bound) is detected (Table 3).

(iii) Tryptic digest of **2**·hCAII^{E69C}, **2**·hCAII^{I91C}, and **2**·hCAII$^{N67G\text{-}E69R\text{-}I91C}$ revealed that the fragments containing the cysteine had a modification of ∼675 Da (Table S7, Figures S31−S34). The modification of 675 Da corresponds to the cofactor lacking Cl, as observed for both native and denaturing MS. Furthermore, the modification of ∼675 Da was detected either for the fragment containing C69 (for **2**·hCAII^{E69C}) or C91 (for **2**·hCAII^{I91C} and **2**·hCAII$^{N67G\text{-}E69R\text{-}I91C}$). Again here, the modification was observed even in the absence of UV light. In contrast, analysis of **2**·hCAII^{WT} digested by trypsin did not reveal any peptide containing a modification of ∼675 Da.

From this data, we conclude that the sulfonamide bioconjugation results from the proximity of the aromatic nitro group and the thiol and does not require UV irradiation. It should be noted however that, based on X-ray and MS data, we cannot exclude the formation of a sulfonate rather than a sulfonamide covalent linkage.

To confirm the positive influence of the covalent bioconjugation on catalytic performance, the enantioselective reduction of harmaline **3** was monitored in the presence of **2**·hCAII^{WT}, **2**·hCAII^{E69C}, and **2**·hCAII$^{N67G\text{-}E69R\text{-}I91C}$ (Figure S21). From these data, the following trends emerge:

(i) The catalytic performance (both yield and *ee*) of **2**·hCAII^{WT} and **2**·hCAII^{E69C} is little affected by the incubation time following the mixing of the cofactor **2** and the host hCAII (Figure S21a,b). As revealed by X-ray crystallography (Figure S1c) and MS analysis (Figures S23 and S28), prolonged incubation only leads to partial formation of the sulfonamide covalent linkage in **2**·hCAII^{E69C}.

(ii) In contrast, for **2**·hCAII$^{N67G\text{-}E69R\text{-}I91C}$, the catalytic performance is affected by the incubation time, prior to the addition of substrate **3** and formate. The catalytic performance of the covalently anchored ArM **2**·hCAII$^{N67G\text{-}E69R\text{-}I91C}$ (resulting from 6 h of incubation) clearly outperforms the non-preincubated **2**·hCAII$^{N67G\text{-}E69R\text{-}I91C}$ (Figure S21c).

(iii) As the pH requirements for the bioconjugation step and catalysis differ (pH = 9.4 and 7.4, respectively), the covalent anchor is not formed in significant amounts under catalytic conditions.

We thus conclude that both cofactor localization and catalytic performance of **2**·hCAII$^{N67G\text{-}E69R\text{-}I91C}$ are positively affected by the presence of an additional covalent linkage between the host protein and the catalytically active pianostool cofactor **2**.

SUBSTRATE SCREENING

To evaluate the substrate scope, the purified hCAII mutants were screened for the transfer hydrogenation of various substrates **4**−**11**. The substrates **5**−**7** are derived from *β*-carbolines, and substrates **8**−**11** are from dihydroisoquinoline. Selected results are displayed in Table 4 and the full screening data can be found in the Supporting Information (Tables S9−S17). The same conditions were used for all substrates. Mutants hCAII$^{N62D\text{-}N67L\text{-}E69Y\text{-}I91C}$ and hCAII$^{L60W\text{-}N62D\text{-}N67L\text{-}E69Y\text{-}I91C}$ obtained during the directed evolution were also tested for catalysis. From the screening, the following trends are apparent: All substrates were converted with good TON (>200 for at least one ArM) and with moderate to good enantioselectivity. Substrates with electron-rich substituents give a higher TON compared to electron-poor substrates. Finally, a lower TON gives a lower enantioselectivity. For the model substrate, we investigated the enantioselective reduction of substrate **4** to crispine A. Mutations from the parent hCAII^{I91C} are deleterious for **2**·hCAII$^{N67G\text{-}E69R\text{-}I91C}$ but further mutations at positions N62 and L60 improve the TON (219) and the *ee* (62%) for **2**·hCAII$^{L60F\text{-}N62Y\text{-}N67G\text{-}E69R\text{-}I91C}$ (Table 4, Entry 1). Mutations N67L and E69Y have a positive effect on enantioselectivity (76% *ee*, Supporting Information), and the last generation improved both *ee* (86%) and TON (355) for **2**·hCAII$^{L60W\text{-}N62D\text{-}N67L\text{-}E69Y\text{-}I91C}$ (Table 4, Entry 2). Next, we tested harmalane **5**, whose structure is similar to harmaline **3** but lacks the electron-donating methoxy group in position 7. The ArM **2**·hCAII$^{N62Y\text{-}N67G\text{-}E69R\text{-}I91C}$ gives the best results with complete conversion and good *ee* (500 TON, 87% *ee* (*R*)) (Table 4, Entry 3) highlighting the tolerance toward substitutions on the indole moiety. For the electron-deficient

https://doi.org/10.1021/acscentsci.1c00825
ACS Cent. Sci. 2021, 7, 1874−1884

Table 4. Selected Results of the Substrate Screening in the Presence of Evolved ATHases[a]

	Substrate	Mutants	TON	*ee* (%)
1	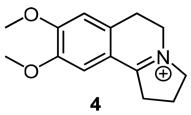 **4**	hCAII$^{L60F-N62Y-N67G-E69R-I91C}$	219	62
2		hCAII$^{L60W-N62D-N67L-E69Y-I91C}$	355	86
3	**5**: R = Me	hCAII$^{N62Y-N67G-E69R-I91C}$	500	87 (*R*)
4		hCAII$^{L60W-N67L-E69Y-I91C}$	189	72 (*S*)
5	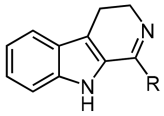 **6**: 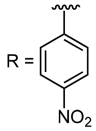	hCAII$^{N67G-E69R-I91C}$	191	80 (*S*)
6		hCAII$^{L60W-N62D-N67L-E69Y-I91C}$	249	72 (*R*)
7	**7**: 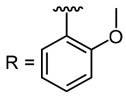	hCAII^{I91C}	296	68 (*S*)
8		hCAII$^{L60W-N62D-N67L-E69Y-I91C}$	372	43 (*R*)
9	**8**: R' = OMe R = Me	hCAII$^{N67L-E69Y-I91C}$	500	59 (*S*)
10		hCAII$^{N62Y-N67G-E69R-I91C}$	422	58 (*R*)
11	**9**: R' = H 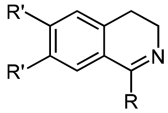 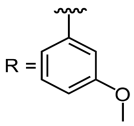	hCAII^{E69C}	250	-56
12		hCAII$^{L60F-N62Y-N67G-E69R-I91C}$	415	-55
13	**10**: R' =H 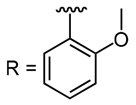	hCAII$^{N62D-N67L-E69Y-I91C}$	338	75
14		hCAII^{E69C}	242	-71
15	**11**: R' =H 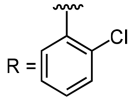	hCAII$^{N62D-N67L-E69Y-I91C}$	215	-51
16		hCAII$^{N62Y-N67G-E69R-I91C}$	47	47

[a]The reactions were performed using cofactor **2** (10 μM), hCAII (10 μM), and substrate (5 mM) in $NaHCO_2$/MOPS buffer (850 mM/340 mM, 25 °C, 16 h). The reported TON and *ee* are the mean values of independent duplicates. Complete screening data are included in the Supporting Information (Tables S9−S17).

harmalane analogue **6**, the TONs decrease compared to substrate **5** (Table S12): **2**·hCAII$^{N67G-E69R-I91C}$ yields the best *ee* (80% (*S*)) and moderate TON (191). Instead, **2**·hCAII$^{L60W-N62D-N67L-E69Y-I91C}$ produces the opposite enantiomer (72% *ee* (*R*), 249 TON) (Entry 5−6).

Interestingly, **2**·hCAII$^{N67G-E69R-I91C}$ is the most selective mutant for harmaline **3** as well as substrate **6**. The reduced activity of the ATHases for this substrate may be traced back to steric hindrance and mismatched electronics caused by the *p*-nitrophenyl group. In contrast, the electron-rich substrate **7** affords higher TONs at the cost of a lower *ee* (Table S13). The best ArM **2**·hCAII^{I91C} gave (*S*)-7-H_2 (296 TON, 68% *ee*, Table 4, Entry 7). Next, we turned our attention to dihydroisoquinolines. The less-hindered substrate **8** gives a high TON but moderate enantioselectivity, with the most enantioselective ArM being **2**·hCAII$^{N67L-E69Y-I91C}$ (500 TON, 59% *ee* (*S*), Table 4, Entry 9). To evaluate the tolerance of transfer hydrogenation toward substrates presenting steric hindrance next to the imine moiety, we tested substrates **9**−**11**.[73] Substrate **9** is reduced with good activities but low stereoselectivity (Table S15). The most promising ArM is **2**·hCAII$^{L60F-N62Y-N67G-E69R-I91C}$ (415 TON, −55% *ee*, Table 4, Entry 12). Next, the steric hindrance was increased by introducing an *o*-methoxyphenyl substituent in substrate **10**. The results (Table S16) are rather different from the previous ones; the mutants derived from **2**·hCAII$^{N67G-E69R-I91C}$ give lower turnovers compared to the mutants derived from **2**·hCAII$^{N67L-E69Y-I91C}$. The best ArM for substrate **10** is **2**·hCAII$^{N62D-N67L-E69Y-I91C}$ (338 TON, 75% *ee*) (Table 4, Entry 13). It should be noted that **2**·hCAII^{E69C} gives the opposite enantiomer (−71% *ee*, 242 TON, Table 4, Entry 14). Finally, substrate **11** incorporating an *o*-chloro substituent was evaluated. In this case, both TON and enantioselectivities are low compared to the other substrates (Table S17) with the most promising catalyst being **2**·hCAII$^{N62D-N67L-E69Y-I91C}$ (Table 4, Entry 15).

CONCLUSION

With the aim of firmly anchoring the Ir-pianostool cofactor **2** within hCAII, we introduced a nucleophilic residue hCAII^{I91C} in the proximity of the *p*-nitropicolinamide ligand bound to the catalytically competent Ir-ion. Rather than affording the anticipated S_NAr reaction, a pyridine−sulfonamide linkage was formed, thus resulting in a dually anchored cofactor. Starting from **2**·hCAII^{I91C}, three rounds of directed evolution were performed using *E. coli* cell surface display. This led to the identification of the (*R*)-selective ATHase **2**·hCAII$^{N67G-E69R-I91C}$ (up to 96% ee and 451 TONs) for tetrahydro-harmine (*R*)-**3**-H_2. The opposite enantiomer (*S*)-**3**-H_2 was obtained using **2**·hCAII$^{N67L-E69Y-I91C}$ (−63% *ee*, 458 TON). We hypothesize that mutation N67G generates more space for the substrate to access the cofactor, whereas the mutation E69R stabilizes the substrate by cation-π interactions.

A substrate scope, carried out with the best mutants, revealed a marked substrate dependency, thus requiring independent directed evolution efforts for each substrate. This suggests that, starting from **2**·hCAII^{I91C}, the evolutionary trajectory has crafted a close fit between the active site and the Ir−H···harmaline transition state, which is less suitable for structurally unrelated substrates. The presence of a single and well-defined cofactor conformation within hCAII resulting from the dual anchor leads to increased TONs and an improved enantioselectivity. Locking the cofactor in place via

https://doi.org/10.1021/acscentsci.1c00825
ACS Cent. Sci. 2021, 7, 1874−1884

an additional covalent bond allows randomizing neighboring amino acids to improve catalytic performance without affecting the position of the cofactor. Accordingly, an ArM with a dual anchor is a propitious starting point for a directed evolution campaign. Finally, the unanticipated reaction between an aromatic nitro group and a cysteine is a welcome addition to the well-established cysteine bioconjugation tools.

■ ASSOCIATED CONTENT

Supporting Information

The Supporting Information is available free of charge at https://pubs.acs.org/doi/10.1021/acscentsci.1c00825.

Detailed experimental procedures; methods for cofactor and substrate synthesis, library construction, protein expression and crystallization, catalysis, MS analysis; data for catalysis, X-ray structures; spectra for MS and NMR (PDF)

■ AUTHOR INFORMATION

Corresponding Authors

Yoann Cotelle − *Aix-Marseille Université, CNRS, Centrale Marseille, iSm2, 13284 Marseille, France*; Email: yoann.cotelle@univ-amu.fr

Johannes G. Rebelein − *Max Planck Institute for Terrestrial Microbiology, D-35043 Marburg, Germany*; orcid.org/0000-0003-2560-716X; Email: Johannes.Rebelein@mpi-marburg.mpg.de

Thomas R. Ward − *Department of Chemistry, University of Basel, 4058 Basel, Switzerland; National Center of Competence in Research "Molecular Systems Engineering", 4058 Basel, Switzerland*; orcid.org/0000-0001-8602-5468; Email: thomas.ward@unibas.ch

Authors

Alina Stein − *Department of Chemistry, University of Basel, 4058 Basel, Switzerland; National Center of Competence in Research "Molecular Systems Engineering", 4058 Basel, Switzerland*

Dongping Chen − *Department of Chemistry, University of Basel, 4058 Basel, Switzerland; National Center of Competence in Research "Molecular Systems Engineering", 4058 Basel, Switzerland*

Nico V. Igareta − *Department of Chemistry, University of Basel, 4058 Basel, Switzerland; National Center of Competence in Research "Molecular Systems Engineering", 4058 Basel, Switzerland*

Complete contact information is available at: https://pubs.acs.org/10.1021/acscentsci.1c00825

Author Contributions

‖A.S. and D.C. contributed equally to this study.

Notes

The authors declare no competing financial interest.

■ ACKNOWLEDGMENTS

T.R.W. thanks the Swiss National Science Foundation (Grant SNF, 200020_182046/1), the NCCR "Molecular Systems Engineering", and the ERC (the DrEAM, Advanced Grant 694424) for generous support of this work. J.G.R. thanks the EMBO for a long-term fellowship (ALTF 194-2017). Dr. Valentin Köhler is thanked for providing the substrate **4**. Dr. Alexandria Deliz Liang is thanked for helpful discussions for the construction of the mutant libraries. Dr. Roman Jakob is thanked for discussions about X-ray crystallography and structure solution, and the staff at beamline X06DA of the Swiss Light Source (Villigen, CH) are thanked for excellent assistance with diffraction data collection. Dr. Witold Szymanski is thanked for the mass spectrometry analysis of the tryptic digest.

■ REFERENCES

(1) Bornscheuer, U. T. The fourth wave of biocatalysis is approaching. *Philos. Trans. R. Soc., A* **2018**, *376*, 1−7.

(2) Hammer, S. C.; Knight, A. M.; Arnold, F. H. Design and evolution of enzymes for non-natural chemistry. *Curr. Opin. Green Sustain. Chem.* **2017**, *7*, 23−30.

(3) Sabatino, V.; Rebelein, J. G.; Ward, T. R. "Close-to-release": Spontaneous bioorthogonal uncaging resulting from ring-closing metathesis. *J. Am. Chem. Soc.* **2019**, *141*, 17048−17052.

(4) Wu, S.; Zhou, Y.; Gerngross, D.; Jeschek, M.; Ward, T. R. Chemo-enzymatic cascades to produce cycloalkenes from bio-based resources. *Nat. Commun.* **2019**, *10*, 5060.

(5) Chordia, S.; Narasimhan, S.; Lucini Paioni, A.; Baldus, M.; Roelfes, G. In vivo assembly of artificial metalloenzymes and application in whole-cell biocatalysis*. *Angew. Chem., Int. Ed.* **2021**, *60*, 5913−5920.

(6) Himiyama, T.; Okamoto, Y. Artificial metalloenzymes: From selective chemical transformations to biochemical applications. *Molecules* **2020**, *25*, 2989.

(7) Booth, R. L.; Grogan, G.; Wilson, K. S.; Duhme-Klair, A.-K. Artificial imine reductases: Developments and future directions. *RSC Chem. Biol.* **2020**, *1*, 369−378.

(8) Leveson-Gower, R. B.; Zhou, Z.; Drienovská, I.; Roelfes, G. Unlocking iminium catalysis in artificial enzymes to create a friedel−crafts alkylase. *ACS Catal.* **2021**, *11*, 6763−6770.

(9) Studer, S.; Hansen, D. A.; Pianowski, Z. L.; Mittl, P. R. E.; Debon, A.; Guffy, S. L.; Der, B. S.; Kuhlman, B.; Hilvert, D. Evolution of a highly active and enantiospecific metalloenzyme from short peptides. *Science* **2018**, *362*, 1285−1288.

(10) Markel, U.; Sauer, D. F.; Schiffels, J.; Okuda, J.; Schwaneberg, U. Towards the evolution of artificial metalloenzymes-a protein engineer's perspective. *Angew. Chem., Int. Ed.* **2019**, *58*, 4454−4464.

(11) Raines, D. J.; Clarke, J. E.; Blagova, E. V.; Dodson, E. J.; Wilson, K. S.; Duhme-Klair, A. K. Redox-switchable siderophore anchor enables reversible artificial metalloenzyme assembly. *Nat. Catal.* **2018**, *1*, 680−688.

(12) Large, B.; Baranska, N. G.; Booth, R. L.; Wilson, K. S.; Duhme-Klair, A.-K. Artificial metalloenzymes: The powerful alliance between protein scaffolds and organometallic catalysts. *Curr. Opin. Green Sustain. Chem.* **2021**, *28*, 100420.

(13) Morra, S.; Pordea, A. Biocatalyst-artificial metalloenzyme cascade based on alcohol dehydrogenase. *Chem. Sci.* **2018**, *9*, 7447−7454.

(14) Thiel, A.; Sauer, D. F.; Markel, U.; Mertens, M. A. S.; Polen, T.; Schwaneberg, U.; Okuda, J. An artificial ruthenium-containing beta-barrel protein for alkene-alkyne coupling reaction. *Org. Biomol. Chem.* **2021**, *19*, 2912−2916.

(15) Markel, U.; Sauer, D. F.; Wittwer, M.; Schiffels, J.; Cui, H.; Davari, M. D.; Kröckert, K. W.; Herres-Pawlis, S.; Okuda, J.; Schwaneberg, U. Chemogenetic evolution of a peroxidase-like artificial metalloenzyme. *ACS Catal.* **2021**, *11*, 5079−5087.

(16) Doble, M. V.; Obrecht, L.; Joosten, H.-J.; Lee, M.; Rozeboom, H. J.; Branigan, E.; Naismith, J. H.; Janssen, D. B.; Jarvis, A. G.; Kamer, P. C. J. Engineering thermostability in artificial metalloenzymes to increase catalytic activity. *ACS Catal.* **2021**, *11*, 3620−3627.

(17) Yang, H.; Srivastava, P.; Zhang, C.; Lewis, J. C. A general method for artificial metalloenzyme formation through strain-promoted azide-alkyne cycloaddition. *ChemBioChem* **2014**, *15*, 223−227.

(18) Sauer, D. F.; Himiyama, T.; Tachikawa, K.; Fukumoto, K.; Onoda, A.; Mizohata, E.; Inoue, T.; Bocola, M.; Schwaneberg, U.; Hayashi, T.; et al. A highly active biohybrid catalyst for olefin metathesis in water: Impact of a hydrophobic cavity in a β-barrel protein. *ACS Catal.* **2015**, *5*, 7519−7522.
(19) Haquette, P.; Salmain, M.; Svedlung, K.; Martel, A.; Rudolf, B.; Zakrzewski, J.; Cordier, S.; Roisnel, T.; Fosse, C.; Jaouen, G. Cysteine-specific, covalent anchoring of transition organometallic complexes to the protein papain from carica papaya. *ChemBioChem* **2007**, *8*, 224−231.
(20) Ricoux, R.; Dubuc, R.; Dupont, C.; Marechal, J. D.; Martin, A.; Sellier, M.; Mahy, J. P. Hemozymes peroxidase activity of artificial hemoproteins constructed from the streptomyces lividans xylanase a and iron(iii)-carboxy-substituted porphyrins. *Bioconjugate Chem.* **2008**, *19*, 899−910.
(21) Rondot, L.; Girgenti, E.; Oddon, F.; Marchi-Delapierre, C.; Jorge-Robin, A.; Ménage, S. Catalysis without a headache: Modification of ibuprofen for the design of artificial metalloenzyme for sulfide oxidation. *J. Mol. Catal. A: Chem.* **2016**, *416*, 20−28.
(22) Song, W. J.; Tezcan, F. A. A designed supramolecular protein assembly with in vivo enzymatic activity. *Science* **2014**, *346*, 1525−1528.
(23) Sano, Y.; Onoda, A.; Hayashi, T. A hydrogenase model system based on the sequence of cytochrome c: Photochemical hydrogen evolution in aqueous media. *Chem. Commun.* **2011**, *47*, 8229−8231.
(24) Sommer, D. J.; Vaughn, M. D.; Ghirlanda, G. Protein secondary-shell interactions enhance the photoinduced hydrogen production of cobalt protoporphyrin ix. *Chem. Commun.* **2014**, *50*, 15852−15855.
(25) Soltau, S. R.; Dahlberg, P. D.; Niklas, J.; Poluektov, O. G.; Mulfort, K. L.; Utschig, L. M. Ru-protein-co biohybrids designed for solar hydrogen production: Understanding electron transfer pathways related to photocatalytic function. *Chem. Sci.* **2016**, *7*, 7068−7078.
(26) Natoli, S. N.; Hartwig, J. F. Noble-metal substitution in hemoproteins: an emerging strategy for biological Catalysis. *Acc. Chem. Res.* **2019**, *52*, 326−335.
(27) Coleman, J. E. Metal ion dependent binding of sulphonamide to carbonic anhydrase. *Nature* **1967**, *214*, 193−194.
(28) Schwizer, F.; Okamoto, Y.; Heinisch, T.; Gu, Y.; Pellizzoni, M. M.; Lebrun, V.; Reuter, R.; Kohler, V.; Lewis, J. C.; Ward, T. R. Artificial metalloenzymes: Reaction scope and optimization strategies. *Chem. Rev.* **2018**, *118*, 142−231.
(29) Durrenberger, M.; Heinisch, T.; Wilson, Y. M.; Rossel, T.; Nogueira, E.; Knorr, L.; Mutschler, A.; Kersten, K.; Zimbron, M. J.; Pierron, J.; et al. Artificial transfer hydrogenases for the enantioselective reduction of cyclic imines. *Angew. Chem., Int. Ed.* **2011**, *50*, 3026−3029.
(30) Carey, J. R.; Ma, S. K.; Pfister, T. D.; Garner, D. K.; Kim, H. K.; Abramite, J. A.; Wang, Z.; Guo, Z.; Lu, Y. A site-selective dual anchoring strategy for artificial metalloprotein design. *J. Am. Chem. Soc.* **2004**, *126*, 10812−10813.
(31) Garner, D. K.; Liang, L.; Barrios, D. A.; Zhang, J. L.; Lu, Y. Covalent anchor positions play an important role in tuning catalytic properties of a rationally designed mnsalen-containing metalloenzyme. *ACS Catal.* **2011**, *1*, 1083−1089.
(32) Laureanti, J. A.; Ginovska, B.; Buchko, G. W.; Schenter, G. K.; Hebert, M.; Zadvornyy, O. A.; Peters, J. W.; Shaw, W. J. A positive charge in the outer coordination sphere of an artificial enzyme increases co2 hydrogenation. *Organometallics* **2020**, *39*, 1532−1544.
(33) Roelfes, G. Lmrr: A privileged scaffold for artificial metalloenzymes. *Acc. Chem. Res.* **2019**, *52*, 545−556.
(34) Zhou, Z.; Roelfes, G. Synergistic catalysis in an artificial enzyme by simultaneous action of two abiological catalytic sites. *Nat. Catal.* **2020**, *3*, 289−294.
(35) Drienovska, I.; Rioz-Martinez, A.; Draksharapu, A.; Roelfes, G. Novel artificial metalloenzymes by in vivo incorporation of metal-binding unnatural amino acids. *Chem. Sci.* **2015**, *6*, 770−776.
(36) Zimbron, J. M.; Heinisch, T.; Schmid, M.; Hamels, D.; Nogueira, E. S.; Schirmer, T.; Ward, T. R. A dual anchoring strategy for the localization and activation of artificial metalloenzymes based on the biotin-streptavidin technology. *J. Am. Chem. Soc.* **2013**, *135*, 5384−5388.
(37) Heinisch, T.; Pellizzoni, M.; Durrenberger, M.; Tinberg, C. E.; Kohler, V.; Klehr, J.; Haussinger, D.; Baker, D.; Ward, T. R. Improving the catalytic performance of an artificial metalloenzyme by computational design. *J. Am. Chem. Soc.* **2015**, *137*, 10414−10419.
(38) Monnard, F. W.; Nogueira, E. S.; Heinisch, T.; Schirmer, T.; Ward, T. R. Human carbonic anhydrase ii as host protein for the creation of artificial metalloenzymes: The asymmetric transfer hydrogenation of imines. *Chem. Sci.* **2013**, *4*, 3269−3274.
(39) Rebelein, J. G.; Cotelle, Y.; Garabedian, B.; Ward, T. R. Chemical optimization of whole-cell transfer hydrogenation using carbonic anhydrase as host protein. *ACS Catal.* **2019**, *9*, 4173−4178.
(40) Zhao, J.; Kajetanowicz, A.; Ward, T. R. Carbonic anhydrase ii as host protein for the creation of a biocompatible artificial metathesase. *Org. Biomol. Chem.* **2015**, *13*, 5652−5655.
(41) Krishnamurthy, V. M.; Kaufman, G. K.; Urbach, A. R.; Gitlin, I.; Gudiksen, K. L.; Weibel, D. B.; Whitesides, G. M. Carbonic anhydrase as a model for biophysical and physical-organic studies of proteins and protein-ligand binding. *Chem. Rev.* **2008**, *108*, 946−1051.
(42) DiMario, R. J.; Machingura, M. C.; Waldrop, G. L.; Moroney, J. V. The many types of carbonic anhydrases in photosynthetic organisms. *Plant Sci.* **2018**, *268*, 11−17.
(43) Hou, G. H.; Xie, J. H.; Yan, P. C.; Zhou, Q. L. Iridium-catalyzed asymmetric hydrogenation of cyclic enamines. *J. Am. Chem. Soc.* **2009**, *131*, 1366−1367.
(44) Leipold, F.; Hussain, S.; Ghislieri, D.; Turner, N. J. Asymmetric reduction of cyclic imines catalyzed by a whole-cell biocatalyst containing an (s)-imine reductase. *ChemCatChem* **2013**, *5*, 3505−3508.
(45) Schrittwieser, J. H.; Velikogne, S.; Kroutil, W. Biocatalytic imine reduction and reductive amination of ketones. *Adv. Synth. Catal.* **2015**, *357*, 1655−1685.
(46) Marshall, J. R.; Yao, P.; Montgomery, S. L.; Finnigan, J. D.; Thorpe, T. W.; Palmer, R. B.; Mangas-Sanchez, J.; Duncan, R. A. M.; Heath, R. S.; Graham, K. M.; et al. Screening and characterization of a diverse panel of metagenomic imine reductases for biocatalytic reductive amination. *Nat. Chem.* **2021**, *13*, 140−148.
(47) Mitsukura, K.; Suzuki, M.; Shinoda, S.; Kuramoto, T.; Yoshida, T.; Nagasawa, T. Purification and characterization of a novel (r)-imine reductase from streptomyces sp. Gf3587. *Biosci., Biotechnol., Biochem.* **2011**, *75*, 1778−1782.
(48) Aleku, G. A.; France, S. P.; Man, H.; Mangas-Sanchez, J.; Montgomery, S. L.; Sharma, M.; Leipold, F.; Hussain, S.; Grogan, G.; Turner, N. J. A reductive aminase from aspergillus oryzae. *Nat. Chem.* **2017**, *9*, 961−969.
(49) Abrahamson, M. J.; Vazquez-Figueroa, E.; Woodall, N. B.; Moore, J. C.; Bommarius, A. S. Development of an amine dehydrogenase for synthesis of chiral amines. *Angew. Chem., Int. Ed.* **2012**, *51*, 3969−3972.
(50) France, S. P.; Howard, R. M.; Steflik, J.; Weise, N. J.; Mangas-Sanchez, J.; Montgomery, S. L.; Crook, R.; Kumar, R.; Turner, N. J. Identification of novel bacterial members of the imine reductase enzyme family that perform reductive amination. *ChemCatChem* **2018**, *10*, 510−514.
(51) Roiban, G.-D.; Kern, M.; Liu, Z.; Hyslop, J.; Tey, P. L.; Levine, M. S.; Jordan, L. S.; Brown, K. K.; Hadi, T.; Ihnken, L. A. F.; et al. Efficient biocatalytic reductive aminations by extending the imine reductase toolbox. *ChemCatChem* **2017**, *9*, 4475−4479.
(52) Cabrero-Antonino, J. R.; Adam, R.; Papa, V.; Beller, M. Homogeneous and heterogeneous catalytic reduction of amides and related compounds using molecular hydrogen. *Nat. Commun.* **2020**, *11*, 3893.
(53) Tin, S.; Fanjul, T.; Clarke, M. L. Hydrogenation of unactivated enamines to tertiary amines: Rhodium complexes of fluorinated phosphines give marked improvements in catalytic activity. *Beilstein J. Org. Chem.* **2015**, *11*, 622−627.

https://doi.org/10.1021/acscentsci.1c00825
ACS Cent. Sci. 2021, 7, 1874−1884

(54) Liu, Y.; Yue, X.; Luo, C.; Zhang, L.; Lei, M. Mechanisms of ketone/imine hydrogenation catalyzed by transition-metal complexes. *EEM* **2019**, *2*, 292−312.
(55) Agouridas, V.; El Mahdi, O.; Diemer, V.; Cargoet, M.; Monbaliu, J. M.; Melnyk, O. Native chemical ligation and extended methods: Mechanisms, catalysis, scope, and limitations. *Chem. Rev.* **2019**, *119*, 7328−7443.
(56) Friedmann, E.; Marrian, D. H.; Simonreuss, I. Antimitotic action of maleimide and related substances. *Br. J. Pharmacol. Chemother.* **1949**, *4*, 105−108.
(57) Gempf, K. L.; Butler, S. J.; Funk, A. M.; Parker, D. Direct and selective tagging of cysteine residues in peptides and proteins with 4-nitropyridyl lanthanide complexes. *Chem. Commun.* **2013**, *49*, 9104−9106.
(58) Moore, E. J.; Zorine, D.; Hansen, W. A.; Khare, S. D.; Fasan, R. Enzyme stabilization via computationally guided protein stapling. *Proc. Natl. Acad. Sci. U. S. A.* **2017**, *114*, 12472−12477.
(59) Goddard, D. R.; Michaelis, L. Derivatives of keratin. *J. Biol. Chem.* **1935**, *112*, 361−371.
(60) Chalker, J. M.; Gunnoo, S. B.; Boutureira, O.; Gerstberger, S. C.; Fernández-González, M.; Bernardes, G. J. L.; Griffin, L.; Hailu, H.; Schofield, C. J.; Davis, B. G. Methods for converting cysteine to dehydroalanine on peptides and proteins. *Chem. Sci.* **2011**, *2*, 1666−1676.
(61) Toda, N.; Asano, S.; Barbas, C. F., 3rd Rapid, stable, chemoselective labeling of thiols with julia-kocienski-like reagents: A serum-stable alternative to maleimide-based protein conjugation. *Angew. Chem., Int. Ed.* **2013**, *52*, 12592−12596.
(62) Ngo, A. H.; Ibanez, M.; Do, L. H. Catalytic hydrogenation of cytotoxic aldehydes using nicotinamide adenine dinucleotide (nadh) in cell growth media. *ACS Catal.* **2016**, *6*, 2637−2641.
(63) Ngo, A. H.; Do, L. H. Structure−activity relationship study of half-sandwich metal complexes in aqueous transfer hydrogenation catalysis. *Inorg. Chem. Front.* **2020**, *7*, 583−591.
(64) Arnold, F. H. Innovation by evolution: Bringing new chemistry to life (nobel lecture). *Angew. Chem., Int. Ed.* **2019**, *58*, 14420−14426.
(65) Cho, I.; Jia, Z. J.; Arnold, F. H. Site-selective enzymatic ch amidation for synthesis of diverse lactams. *Science* **2019**, *364*, 575−578.
(66) Basler, S.; Studer, S.; Zou, Y.; Mori, T.; Ota, Y.; Camus, A.; Bunzel, H. A.; Helgeson, R. C.; Houk, K. N.; Jimenez-Oses, G.; et al. Efficient lewis acid catalysis of an abiological reaction in a de novo protein scaffold. *Nat. Chem.* **2021**, *13*, 231−235.
(67) Robles, V. M.; Durrenberger, M.; Heinisch, T.; Lledos, A.; Schirmer, T.; Ward, T. R.; Marechal, J. D. Structural, kinetic, and docking studies of artificial imine reductases based on biotin-streptavidin technology: An induced lock-and-key hypothesis. *J. Am. Chem. Soc.* **2014**, *136*, 15676−15683.
(68) Tang, L.; Gao, H.; Zhu, X.; Wang, X.; Zhou, M.; Jiang, R. Construction of "small-intelligent" focused mutagenesis libraries using well-designed combinatorial degenerate primers. *BioTechniques* **2012**, *52*, 149−158.
(69) Kachur, A. V.; Koch, C. J.; Biaglow, J. E. Mechanism of copper-catalyzed oxidation of glutathione. *Free Radical Res.* **1998**, *28*, 259−269.
(70) Ngamchuea, K.; Batchelor-McAuley, C.; Compton, R. G. The copper(ii)-catalyzed oxidation of glutathione. *Chem. - Eur. J.* **2016**, *22*, 15937−15944.
(71) Harpaz, Y.; Gerstein, M.; Chothia, C. Volume changes on protein folding. *Structure* **1994**, *2*, 641−649.
(72) Fleming, S. A.; Rawlins, D. B.; Samano, V.; Robins, M. J. Photochemistry of nucleoside transport inhibitor 6-s-benzylated thiopurine ribonucleosides. Implications for a new class of photoaffinity labels. *J. Org. Chem.* **1992**, *57*, 5968−5976.
(73) Barrios-Rivera, J.; Xu, Y.; Wills, M. Asymmetric transfer hydrogenation of unhindered and non-electron-rich 1-aryl dihydroisoquinolines with high enantioselectivity. *Org. Lett.* **2020**, *22*, 6283−6287.

https://doi.org/10.1021/acscentsci.1c00825
ACS Cent. Sci. 2021, 7, 1874−1884